Direct Bandgap Transition in Many-Layer MoS_2 by Plasma-Induced Layer Decoupling

Rohan Dhall, Mahesh R. Neupane, Darshana Wickramaratne, Matthew Mecklenburg, Zhen Li, Cameron Moore, Roger K. Lake, and Stephen Cronin**

2D materials, such as graphene and few-layer transition metal dichalcogenides (TMDCs), have attracted great research interest in the past decade, since mechanical exfoliation of these materials from their 3D bulk counterparts was demonstrated.[1] Graphene, in particular, is of tremendous interest from a scientific standpoint due to its linear band dispersion,[2] and excellent carrier mobility,[3] allowing observation of phenomena such as the quantum hall effect,[4–6] non-adiabatic phonon anomalies,[7] and Dirac fermion nature of electrons.[7,8] However, due to its gapless dispersion, its utility in the field of optoelectronics is limited. TMDCs, such as MoS_2, WS_2, and WSe_2, on the other hand, are found to exist in similar layered structures and exhibit finite bandgaps in the visible wavelength range.[9–11] TMDCs have traditionally been used as lubricants and host materials for intercalation compounds.[12,13] The optical properties of these TMDCs vary significantly with layer thickness.[11] While monolayer MoS_2 and WSe_2 are direct bandgap materials, their few-layer counterparts are indirect semiconductors, which show a greatly suppressed photoluminescence (PL).[11,14] Consequently, most recent research efforts have been directed towards monolayer TMDCs. Monolayers, while direct bandgap, have small optical densities, which limits their potential use in practical devices.

In the work presented here, a gentle oxygen plasma treatment is shown to produce a direct bandgap transition in many-layer MoS_2.The band structure of MoS_2 with more than four layers in thickness is almost identical to that of bulk MoS_2, and flakes thicker than that are considered "many layer" in this work. The data gathered in this work were obtained from samples with thicknesses up to 15 layers (approximately 12 nm), and approximately 5–15 μm in size. This transition is studied using PL spectroscopy, Raman spectroscopy, atomic force microscopy (AFM), and electron energy loss spectroscopy (EELS). Ab initio calculations provide a clear insight into the layer decoupling mechanism responsible for this indirect-to-direct gap transition.

Low-power, remote (or downstream) plasma treatment has been effectively used to remove hydrocarbon impurities in situations where the sample itself is known to be susceptible to damage by fast-moving ionic species.[15] For example, remote plasma has been used to selectively etch away metallic carbon nanotubes and surface contaminants, to enable fabrication of semiconducting single-wall carbon nanotube field effect transistors.[16] We use an XEI Evactron Soft Clean plasma cleaner, in which the plasma is generated by flowing room air past an electrode supplied with 20 W of RF power at 200 mTorr. The sample is placed a certain distance (6–10 cm) away from the plasma source, and ionized oxygen atoms diffuse towards the sample chamber with low kinetic energies. Samples were exposed to the O_2 plasma for about 3 min. While typical plasma cleaners used in semiconductor fabrication operate using a "sputtering" mechanism, wherein the sample is bombarded with ions carrying significant kinetic energy, remote plasma cleaners rely mainly on the chemical reactivity of the ionized oxygen to remove surface contaminants. Despite the presence of nitrogen in the gas mixture, the plasma itself mainly consists of oxygen radicals, since the N_2 molecule has a much higher bonding energy.

Figure 1 shows the optical microscope image of a mechanically exfoliated flake of MoS_2 on an oxidized silicon wafer. The PL spectra of these flakes are obtained using a 532 nm excitation laser focused to a 0.5 μm spot, attenuated in power to 10 $\mu W\ \mu m^{-2}$, to minimize sample heating. The PL spectra of the same MoS_2 flake taken before and after 3 min of oxygen plasma treatment are shown in Figure 1c. The two peaks labeled A and B correspond to transitions between the conduction band and the two (spin–orbit split) valence bands at the K point in the Brillouin zone. In this particular case, there is a 16-fold enhancement of the PL intensity after the oxygen plasma treatment, along with significant (about 46%) narrowing of the spectral linewidth, indicating an improvement in material quality. The PL peak also shifts from typical energies between 1.81 and 1.83 eV before O_2 plasma to 1.86 eV after the plasma treatment. This is consistent with the observations of Mak et al.[11] on suspended, monolayer, direct gap MoS_2. Table S1 (Supporting Information) provides a list of PL peak positions and linewidths

R. Dhall, Z. Li, Prof. S. Cronin
Ming Hsieh Department of Electrical Engineering
University of Southern California
Los Angeles, CA 90089, USA
E-mail: scronin@usc.edu
R. Dhall, Dr. M. Mecklenburg
Center for Electron Microscopy and Microanalysis
University of Southern California
Los Angeles, CA 90089, USA
M. R. Neupane, D. Wickramaratne, Prof. R. K. Lake
Laboratory for Terahertz and Terascale Electronics
Department of Electrical and Computer Engineering
University of California
Riverside, CA 92521, USA
E-mail: rlake@ee.ucr.edu
C. Moore
XEI Scientific
Redwood City, CA 94063, USA

DOI: 10.1002/adma.201405259

ADVANCED MATERIALS
www.advmat.de

www.MaterialsViews.com

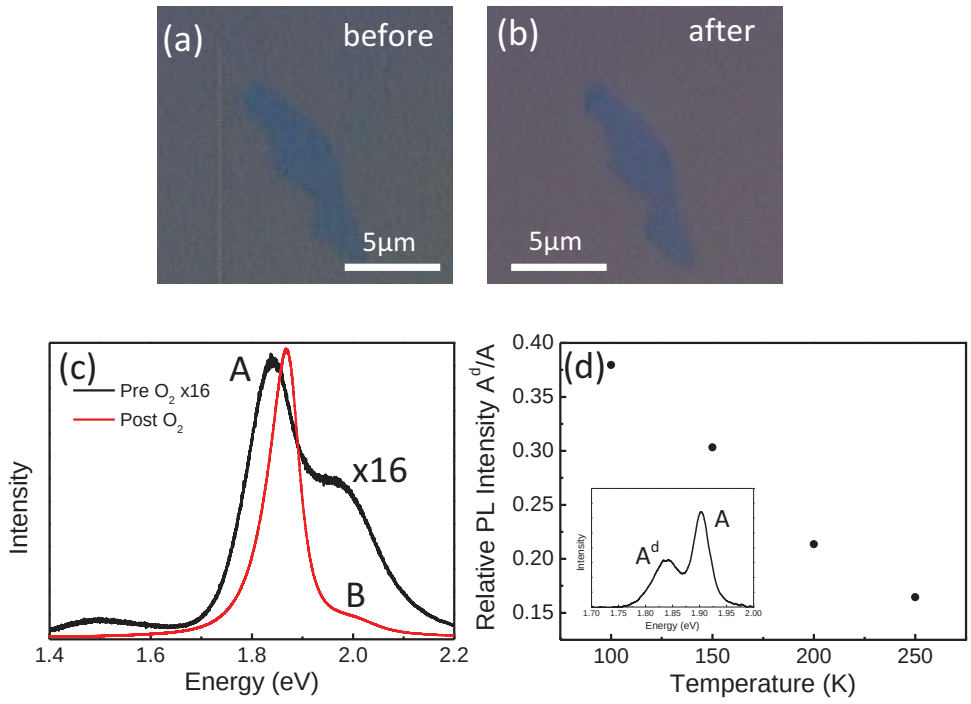

Figure 1. Optical microscope image of a few layer MoS_2 flake (a) before and (b) after 3 min of oxygen plasma treatment. c) PL spectra before and after oxygen plasma treatment, plotted on different scales, highlighting the blueshift of the A exciton, the narrowing of the spectral linewidth, and the emergence of the asymmetry in PL lineshape after plasma treatment at 300 K. d) Inset shows the emergence of a distinct, low-energy peak at 100 K. The relative intensity of the low-energy PL peak is shown as a function of temperature.

measured before and after oxygen plasma treatment for 35 MoS_2 flakes measured in this study. We observed enhanced PL intensities for 32 out of 35 many-layer MoS_2 flakes tested, indicating that this method is robust and scalable.

The large intensity enhancement and blueshift of the PL peak observed after oxygen treatment are not the result of a reduction in the layer thickness of the MoS_2, as shown by AFM and Raman measurements. The AFM images taken before and after oxygen treatment, surprisingly, reveal an increase in flake thickness, as shown in **Figure 2**c. The error in our height measurements can be estimated from the standard deviation of the measured profile on the underlying SiO_2 substrate, which is found to be 2.4 Å both before and after plasma treatment. For the AFM data shown in Figure 2c, the step height along the white dashed lines in Figure 2a,b increases by about 20 ± 5 Å due to the treatment with oxygen plasma. The 20 Å increase in the film thickness, distributed across the 9 nm MoS_2 film consisting of 11 to 13 monolayers, corresponds to an average increase in each van der Waals (vdW) gap of 1.5–1.8 Å. Density functional theory (DFT) calculations described below show that this increased interlayer distance is sufficient to cause an indirect-to-direct bandgap transition suggesting that the enhanced PL observed is the result of plasma-assisted layer decoupling of the MoS_2 lattice.

Raman spectra taken before and after oxygen treatment also indicate that no thinning of the sample is occurring. In **Figure 3**c, the Raman spectra of a MoS_2 flake exhibit two peaks corresponding to the E^1_{2g} (in-plane) and A_{1g} (out-of-plane) vibrational modes.[17] The separation between these two peaks provides a good measure of the layer thickness of the material, varying from 19 cm^{-1} for monolayer to 25 cm^{-1} for *N*-layer ($N > 6$) MoS_2.[17] We studied the Raman spectra of 17 flakes of MoS_2, before and after O_2 plasma treatment. On average, the separation between the two Raman peaks reduced from 22.6 to 21.4 cm^{-1} after plasma treatment, indicating that the flakes are still multilayer MoS_2. We consistently see a downshift in the A_{1g} (out-of-plane) Raman mode position and a narrowing of the Raman linewidth. However, no consistent and systematic change of the in-plane (E^1_{2g}) mode is observed, which is also seen to upshift slightly at times. These results indicate that the intralayer spring constant is unaffected by the plasma treatment, and the interlayer spring constant is consistently weakened (albeit by a small amount). This shows that a mere flake thinning is not the mechanism responsible for the enhanced PL intensity observed after O_2 plasma treatment. In contrast, an increase in the flake thickness shown by AFM, and the softening of the interlayer spring constant seen in the Raman spectra, points to a mechanism in which the interlayer vdW coupling is weakened. The reduction in Raman intensity is a possible consequence of the change in lattice symmetry, which determines the matrix elements and selection rules for Raman active vibrational modes. A tabulated summary of our Raman data is given in Table S2 (Supporting Information). While Raman spectroscopy can only differentiate single-layer, bilayer (2L), and trilayer (3L) MoS_2 reliably, our Raman data exclude the possibility that the flake thickness has actually been reduced to monolayer MoS_2.

To explain the observed change in the PL peak with oxygen intercalation, we attribute the emergence of the PL peak at 1.8 eV to an increase in the vdW gap between the adjacent layers

Adv. Mater. **2015**,
DOI: 10.1002/adma.201405259

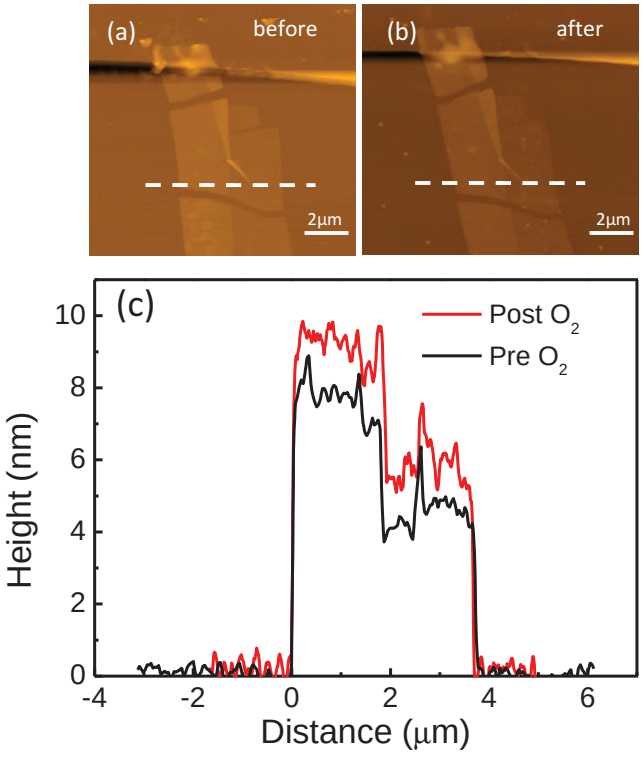

Figure 2. AFM (height) images of a MoS_2 flake taken (a) before and (b) after a 3 min oxygen plasma treatment (plotted on different color scales). The step height profiles along the dashed lines are shown in (c). A significant increase in sample thickness, of about 2 nm, is observed after plasma treatment.

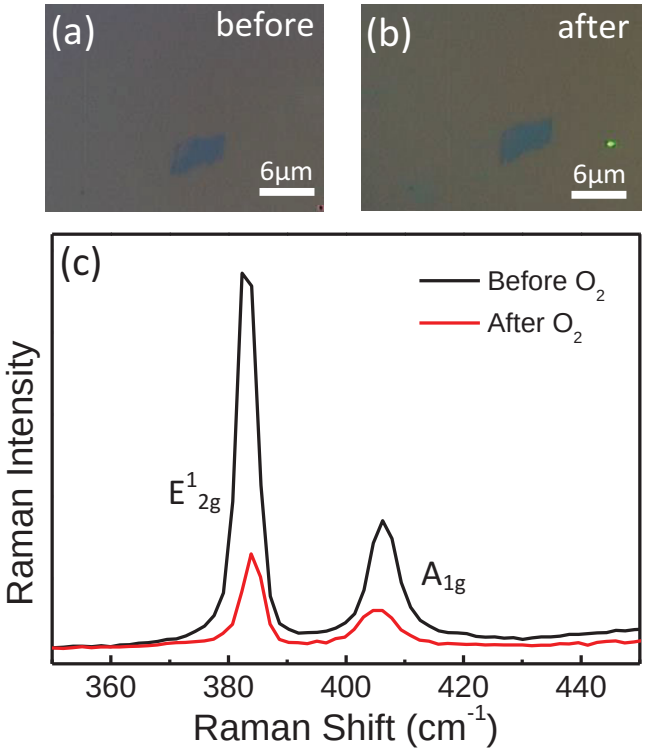

Figure 3. Optical microscope image of a many-layer MoS_2 flake (a) before and (b) after 3 min of oxygen plasma treatment. c) Raman spectra before and after plasma treatment. No significant shift in the Raman peaks is observed, although the Raman intensity for both peaks is reduced, and a slight narrowing of the peaks is observed.

of MoS_2. To support this argument, we calculate the electronic band structure of 2L, 3L, and quad-layer (4L) MoS_2, as shown in **Figure 4**, for a range of vdW gap distances between the adjacent layers. Our calculations are based on first-principles DFT using the projector augmented wave method as implemented in the software package VASP.[18] The screened Heyd–Scuseria–Ernzerhof (HSE) hybrid functional has been employed for this study.[19] Spin–orbit coupling was included self-consistently within the band structure calculations. The HSE calculations incorporate 25% short-range Hartree–Fock exchange, and the screening parameter is set to 0.4 Å.[20] A Monkhorst–Pack scheme was adopted to integrate over the Brillouin zone with a k-mesh $9 \times 9 \times 1$ for the 2L and 3L structures. The k-mesh was reduced to a converged $4 \times 4 \times 1$ grid for the 4L structure HSE calculations. A plane-wave basis kinetic energy cutoff of 300 eV was used. The lattice constants for the 2L and 3L structures are obtained from our prior calculations on the bulk structure of MoS_2 that have been optimized with vdW interactions accounted for using a semi-empirical correction to the Kohn–Sham energies.[21] A vacuum spacing of 15 Å is added along the *z*-axis for all the structures. The atomic coordinates for each structure were optimized in all directions using the DFT-D2 dispersion corrections[22] until all the interatomic forces are below 0.01 eV $Å^{-1}$. The default level of theory in all calculations is HSE with spin–orbit coupling. Only deviations from the defaults are noted. The equilibrium vdW gap, d_{vdW}, is 3.12 Å for the 2L, 3L, and 4L MoS_2 structures.

The valence band edge, Γ_v, is composed of 28% p_z orbitals from the S atoms and 67% d_{z^2} orbitals from Mo atoms. The valence bands at K_v contain no d_{z^2} or p_z components and are primarily composed of d_{x^2} and d_{xy} orbitals. Because of the large p_z orbital component of the S atoms, the Γ_v valley has the largest interlayer coupling and is, therefore, most sensitive to the presence of adjacent layers. When two monolayers are brought together, the Γ_v valleys of the two layers couple and split. At the equilibrium interlayer distance of 3.12 Å, the energy splitting is 620 meV. The corresponding energy splitting at K_v due to interlayer coupling is 74 meV. Thus, the interlayer coupling causes the Γ_v valley to rise above the K_v valley as two monolayers are brought into close proximity.

The orbital composition of the conduction band at K_c is 67% d_{z^2} with no p_z component. The next closest conduction band valley is at Σ_c composed of 36% d_{z^2} and a minor contribution from the p_z orbitals of the S atoms. The conduction band at K_c has no p_z components from the sulfur atoms. Thus, the K_c valley is only weakly affected by the proximity of an adjacent layer, and as two monolayers are brought together, the conduction band remains at K_c for the 2L, 3L, and 4L structures.

The electronic band structures for 2L, 3L, and 4L MoS_2 are calculated for a range of vdW gap distances starting from the equilibrium value of d_{vdW} = 3.12 Å and increasing it up to a maximum of 1.6 times the equilibrium value. When the vdW gap is increased by a factor of 1.6 in a 2L structure, the energy of Γ_v decreases by 470 meV with respect to the vacuum energy.

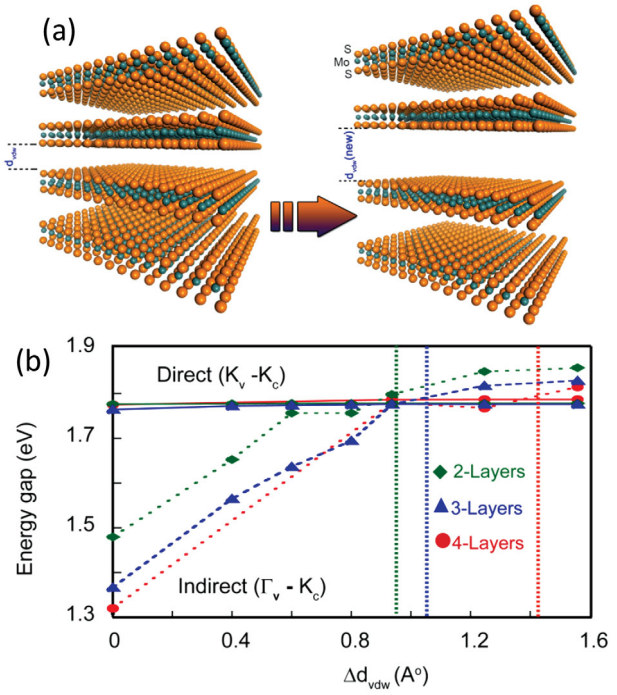

Figure 4. a) Atomistic structure of the 4L MoS_2 with the equilibrium vdW gap, d_{vdw}, and the modified vdW gap, d_{vdw} (new). b) Direct gap (solid) and indirect gap (dotted) energy transitions for 2L, 3L, and 4L MoS_2 for a range of increases in the vdW gap (Δd_{vdw}). The dotted vertical lines indicate the indirect-to-direct transition vdW gaps for 2L (green), 3L (blue), and 4L (red) MoS_2 .

The K_v–K_c direct gap transition changes by only 2 meV. A crossover from an indirect to direct gap transition occurs when the equilibrium vdW gap in 2L, 3L, and 4L MoS_2 is increased by 1.0, 1.13, and 1.45 Å, respectively. At these separation distances, the direct gap and indirect gap energies are equal. With further increases in the vdW gap, the bandgap becomes direct. The direct gap K_v–K_c and the indirect gap Γ_v–K_c bandgap energies calculated using DFT are illustrated for the 2L, 3L, and 4L structures in Figure 4b. The calculated increases in the vdW gaps that produce the indirect-to-direct transition are consistent with the experimentally measured increase in the film thickness shown in Figure 2c.

The consistency between the increase in interlayer separation revealed by AFM and Raman spectroscopy, and the corresponding increase in PL yields with theoretical calculations point to a mechanism in which exposure to oxygen plasma disturbs the interlayer vdW bonding. One scenario which could lead to this effect is intercalation of vdW gap of MoS_2 by a foreign species during expose to oxygen plasma. Electrochemical techniques, using liquid phase solvents, have been shown to enable intercalation of small chemical species (such as lithium ions) into lattices of layered materials like graphite.[23] More recently, such methods have been used to completely separate the individual layers of 2D materials.[24–27] Layer separation is achieved by completely saturating the interlayer gaps in the host TMDC lattice with guest species, followed by mechanical agitation. From intercalation chemistry, we know that a guest species need not distribute itself evenly in the interlayer gaps of the host lattice. It is common to find staging of guest atoms, which is the occupation of every other interlayer gap.[12,13,28] Similarly, the guest species may cover only a fraction of the area in any one interlayer gap, leaving the host atomic layers weakly bound to one another. It would be expected that completely saturating the interlayer spaces with guest species would lead to complete exfoliation of MoS_2. We do indeed see that overexposure of MoS_2 flakes to the plasma treatment sometimes leads to complete removal of the flakes. However, unlike previous liquid-based exfoliation methods, by controlling the plasma treatment parameters, we are able to ensure only partial coverage of the interlayer spaces, and hence prevent complete exfoliation. Figure S2 in the Supporting Information shows the increase in flake thickness for 12 different many-layer MoS_2 flakes. 11 out of 12 flakes show an increase in the thickness after plasma treatment. 10 of these 12 samples showed an increase in the PL intensity. Figure S3 in the Supporting Information shows the PL enhancement factor plotted as a function of the change in flake thickness for these 10 samples.

In MoS_2, such an engineered system is tremendously advantageous for device applications. By reducing the interplanar overlap of electronic states in many-layer MoS_2, one would expect the material to behave as a stack of isolated "monolayer" MoS_2 flakes, each with a direct bandgap desirable for optoelectronic applications. One of the challenges in creating an optoelectronic device such as a p–n junction from a "monolayer" crystal arises from local fluctuations in charge densities due to surface impurities, which precludes controlled doping of the material. The direct bandgap many-layer crystal obtained in this work would be far less susceptible to surface effects. Furthermore, many-layer, direct bandgap MoS_2 would enable cross plane p–n junctions to be fabricated with finite space charge regions, as in conventional p–n junctions. The applicability of this method in decoupling layers is likely limited for significantly thicker flakes, due to the kinetics of the intercalation process. Future studies of the size dependence of this intercalation process, including the possibility of staging, are needed. The intercalation of foreign species appears to be quite stable, and plasma-treated MoS_2 does not revert to its indirect form over time. The presence of foreign species, however, significantly destabilizes the interlayer vdW bonding in the MoS_2, and some delamination of the MoS_2 is observed when stored under ambient conditions over the span of a few weeks. We believe that by applying various strategies for hermetic sealing, this instability can be overcome in practical device applications.

Another aspect of the oxygen plasma treatment, evident from the AFM images in Figure 2 and Figure S1 in the Supporting Information, is the dramatic reduction in surface contaminants arising from lithographic and exfoliation residues, which is expected to contribute to the dramatic increase in PL efficiency shown in Figure 1. The plasma cleaning treatment also leads to a consistent narrowing of the PL linewidth, as evident in Figure 1c. We also observe that while the intensity of the A exciton luminescence is greatly enhanced, the intensity of the B exciton is actually diminished. This is also to be expected, since optically generated higher energy (B) excitons, due to their increased lifetimes, now have more time to find a decay path to the more energetically favorable (A) state before

Adv. Mater. **2015**,
DOI: 10.1002/adma.201405259

radiative recombination. This transition from B to A is disallowed in defect-free MoS_2, since those states are orthonormal. However, oxygen plasma treatment perturbs the crystal potential, thereby allowing this transition, and explaining the reduction of B exciton luminescence. This observed blueshift in the PL peak is consistent with previous studies on suspended MoS_2[11] and MoS_2 passivated by ionic liquids.[29] The lineshape of the observed luminescence from the A exciton is found to be asymmetric, with a significant shift of the spectral weight towards the low-energy side, as shown in Figure 1c. This apparent asymmetry is the result of the emergence of a peak near the low-energy shoulder of the A excitonic peak. PL spectra taken at cryogenic temperatures provide insight into the underlying nature of this lineshape asymmetry. Here, we are able to distinguish the lower energy peak clearly, shown in the inset of Figure 1d. As shown recently by Korn et al.,[30] this peak (labeled A^d) is characteristic of the formation of a localized excitonic state, due to the creation of defects or, alternatively, the emergence of disorder. Figure 1d shows the relative intensity of this low-energy A^d peak to the dominant A exciton peak, as a function of sample temperature. At room temperature, the excitonic state is no longer well localized, leading to a diminished intensity of the observed disorder-related peak. When higher RF power plasmas are used, we observe the emergence of disorder and defects as indicated by the sub-bandgap A^d peak in the PL spectra at room temperature. However, under the optimized conditions used in this work, we do not observe any A^d peak in the PL spectra at room temperature. HRTEM and EELS analysis presented in Figure S4 of the Supporting Information also does not reveal significant flake deterioration, even after several minutes of exposure to remote oxygen plasma. As a consequence of disorder, one would expect the PL intensity to vary spatially. However, in our 2D PL maps, we were unable to detect inhomogeneity of PL intensity over a MoS_2 flake of uniform thickness. We believe that this is because both the exciton radius and the size of any defect state are expected to be at least an order of magnitude smaller than the diffraction limit. While interpretation of far-field optical spectroscopy, as presented in this work, sheds some light on the possible mechanisms at play, more direct evidence may be found by near-field optical studies. Similarly, a more detailed ab initio calculation by including guest species in the vdW gap would prove to be useful.

A recent report in the literature[31] also observes similar PL enhancement, attributed to formation of Mo–O bonds based on XPS signals. However, XPS measurements are ill suited to flakes of MoS_2, as the illuminated spot size is typically 15–20 μm, which is considerably larger than the typical flake size. We believe that such a bond formation should have a dramatic impact on the Raman spectrum, due to a change in the atomic mass. No such shift was observed in our work, hence ruling out Mo–O bond formation.

In summary, we demonstrate an indirect-to-direct bandgap transition in many-layer MoS_2 using a simple, scalable oxygen plasma-induced process. The PL efficiency is found to increase due to the decoupling of electronic states in individual layers. Furthermore, a significant narrowing in spectral linewidth is observed, indicating an increase in the exciton lifetime in MoS_2, due to the removal of surface contaminants. The mechanism for the PL enhancement relies on incomplete filling (or intercalation) of the interlayer gap with a guest species, with a very slight change in doping. While the increase in interlayer separation confines the carriers in two dimensions, the possible creation of defects in MoS_2 likely gives rise to localized excitonic states with longer lifetimes. This simple processing step could have vast implications for future generations of optoelectronic devices by providing direct bandgap TMDCs with large optical densities.

Supporting Information

Supporting Information is available from the Wiley Online Library or from the author.

Acknowledgements

R.D. and Z.L. prepared samples. R.D. and M.H.M. performed the measurements. M.R.N. and D.W. performed the DFT calculations. R.D., M.R.N., D.W., M.H.M., C.M., R.K.L., and S.C. wrote the manuscript. This research was supported by DOE Award No. DE-FG02–07ER46376. The electron microscopy images used in this paper were recorded at the Center for Electron Microscopy and Microanalysis, University of Southern California. M.R.N., D.W., and R.K.L. acknowledge support from the National Science Foundation (NSF) Grant Nos. 1124733 and 1128304 and FAME, one of six centers of STARnet, a Semiconductor Research Corporation program sponsored by MARCO and DARPA. This work used the Extreme Science and Engineering Discovery Environment (XSEDE), which is supported by NSE, Grant No. OCI-1053575, and Information Technology at Purdue University, West Lafayette, IN, USA.

Received: November 17, 2014
Published online:

[1] K. Novoselov, D. Jiang, F. Schedin, T. Booth, V. Khotkevich, S. Morozov, A. Geim, *Proc. Natl. Acad. Sci. USA* **2005**, *102*, 10451.
[2] A. C. Neto, F. Guinea, N. Peres, K. S. Novoselov, A. K. Geim, *Rev. Mod. Phys.* **2009**, *81*, 109.
[3] K. I. Bolotin, K. Sikes, Z. Jiang, M. Klima, G. Fudenberg, J. Hone, P. Kim, H. Stormer, *Solid State Commun.* **2008**, *146*, 351.
[4] Y. Zhang, Y.-W. Tan, H. L. Stormer, P. Kim, *Nature* **2005**, *438*, 201.
[5] A. K. Geim, K. S. Novoselov, *Nat. Mater.* **2007**, *6*, 183.
[6] V. Singh, M. M. Deshmukh, *Phys. Rev. B* **2009**, *80*, 081404.
[7] S. Pisana, M. Lazzeri, C. Casiraghi, K. S. Novoselov, A. K. Geim, A. C. Ferrari, F. Mauri, *Nat. Mater.* **2007**, *6*, 198.
[8] J. Tsang, M. Freitag, V. Perebeinos, J. Liu, P. Avouris, *Nat. Nanotechnol.* **2007**, *2*, 725.
[9] Q. H. Wang, K. Kalantar-Zadeh, A. Kis, J. N. Coleman, M. S. Strano, *Nat. Nanotechnol.* **2012**, *7*, 699.
[10] M. Chhowalla, H. S. Shin, G. Eda, L.-J. Li, K. P. Loh, H. Zhang, *Nat. Chem.* **2013**, *5*, 263.
[11] K. F. Mak, C. Lee, J. Hone, J. Shan, T. F. Heinz, *Phys. Rev. Lett.* **2010**, *105*, 136805.
[12] M. Dresselhaus, *MRS Bull.* **1987**, *12*, 24.
[13] S. M. Whittingham, *Intercalation Chemistry*, Elsevier, **2012**.
[14] A. Splendiani, L. Sun, Y. Zhang, T. Li, J. Kim, C.-Y. Chim, G. Galli, F. Wang, *Nano Lett.* **2010**, *10*, 1271.
[15] B. Anthony, L. Breaux, T. Hsu, S. Banerjee, A. Tasch, *J. Vac. Sci. Technol. B* **1989**, *7*, 621.
[16] G. Zhang, P. Qi, X. Wang, Y. Lu, X. Li, R. Tu, S. Bangsaruntip, D. Mann, L. Zhang, H. Dai, *Science* **2006**, *314*, 974.
[17] C. Lee, H. Yan, L. E. Brus, T. F. Heinz, J. Hone, S. Ryu, *ACS Nano* **2010**, *4*, 2695.

[18] G. Kresse, J. Hafner, *Phys. Rev. B* **1993**, *47*, 558.
[19] J. Heyd, G. E. Scuseria, M. Ernzerhof, *J. Chem. Phys.* **2003**, *118*, 8207.
[20] F. Zahid, L. Liu, Y. Zhu, J. Wang, H. Guo, *AIP Adv.* **2013**, *3*, 052111.
[21] D. Wickramaratne, F. Zahid, R. K. Lake, *J. Chem. Phys.* **2014**, *140*, 124710.
[22] S. Grimme, *J. Comput. Chem.* **2006**, *27*, 1787.
[23] Z. Shu, R. McMillan, J. Murray, *J. Electrochem. Soc.* **1993**, *140*, 922.
[24] V. Nicolosi, M. Chhowalla, M. G. Kanatzidis, M. S. Strano, J. N. Coleman, *Science* **2013**, *340*.
[25] J. N. Coleman, M. Lotya, A. O'Neill, S. D. Bergin, P. J. King, U. Khan, K. Young, A. Gaucher, S. De, R. J. Smith, *Science* **2011**, *331*, 568.
[26] Y. Hernandez, V. Nicolosi, M. Lotya, F. M. Blighe, Z. Sun, S. De, I. McGovern, B. Holland, M. Byrne, Y. K. Gun'Ko, *Nat. Nanotechnol.* **2008**, *3*, 563.
[27] G. Eda, H. Yamaguchi, D. Voiry, T. Fujita, M. Chen, M. Chhowalla, *Nano Lett.* **2011**, *11*, 5111.
[28] G. Wiegers, *Physica B+C (Amsterdam)* **1980**, *99*, 151.
[29] Z. Li, S.-W. Chang, C.-C. Chen, S. B. Cronin, *Nano Res.* **2014**, *7*, 973.
[30] T. Korn, S. Heydrich, M. Hirmer, J. Schmutzler, C. Schüller, *Appl. Phys. Lett.* **2011**, *99*, 102109.
[31] H. Nan, Z. Wang, W. Wang, Z. Liang, Y. Lu, Q. Chen, D. He, P. Tan, F. Miao, X. Wang, *ACS Nano* **2014**, *8*, 5738.

Adv. Mater. **2015**,
DOI: 10.1002/adma.201405259